

# Hyperentangled Time-bin and Polarization Quantum Key Distribution

Joseph C. Chapman,<sup>1,2,\*</sup> Charles C. W. Lim,<sup>3,4</sup> and Paul G. Kwiat<sup>1,2</sup>

<sup>1</sup>*Illinois Quantum Information Science and Technology Center,  
University of Illinois at Urbana-Champaign, Urbana, IL, USA*

<sup>2</sup>*Department of Physics, University of Illinois at Urbana-Champaign, Urbana, IL, USA*

<sup>3</sup>*Department of Electrical & Computer Engineering,  
National University of Singapore, Singapore*

<sup>4</sup>*Centre for Quantum Technologies, National University of Singapore, Singapore*

Fiber-based quantum key distribution (QKD) networks are currently limited without quantum repeaters. Satellite-based QKD links have been proposed to extend the network domain. We have developed a quantum communication system, suitable for realistic satellite-to-ground communication to longer distances. With this system, we have executed an entanglement-based QKD protocol developed by Bennett, Brassard, and Mermin in 1992 (BBM92), achieving quantum bit error rates (QBER) below 2%. More importantly, we demonstrate low QBER execution of a higher dimensional hyperentanglement-based QKD protocol which has a distinct advantage over BBM92, using photons simultaneously entangled in polarization and time-bin. We verify the security of our protocol using a rigorous, finite-key analysis, and show that it is suitable for a space-to-ground link, after incorporating Doppler shift compensation.

## MOTIVATION AND BACKGROUND

Implementing quantum key distribution (QKD) or other quantum communication protocols over long distances is a major goal and challenge for establishing a global quantum network. To lay dedicated dark fiber over long distances is expensive and non-reconfigurable, and, without quantum repeaters, such links have very low transmission. The low transmission is due the exponential scaling of absorption in fiber with distance. It has been proposed to instead use space-based links where there are quantum channels between a ground station

and an orbiting platform [1, 2]. Such a channel has much lower loss than fiber over the same distance, allowing much more efficient protocol execution over comparable distances; for example, the recent achievement of entanglement distribution from a satellite to two ground stations realized a loss reduction of some 12 orders of magnitude [3], though the detection rate and signal-to-noise ratio were far too low for secure QKD. Also, the same satellite demonstrated decoy-state QKD, realizing a 20 orders of magnitude enhancement in channel transmission [4]. A number of other groups around the world are also working on similar endeavors [5–8]. Here we investigate polarization entanglement-based QKD (specifically, the BBM92 protocol [9]) as well as a higher dimensional, hyperentanglement-based QKD (HEQKD) protocol, including a finite-key security analysis. See S.I. for BBM92 protocol, results, finite-key analysis and discussion.

We consider an entanglement-based ( $d = 4$ ) QKD protocol with four measurement bases. Alice and Bob share the initial state

$$|\Psi_{AB}\rangle = \frac{1}{2}(|00\rangle + |11\rangle + |22\rangle + |33\rangle). \quad (1)$$

Alice' and Bob's bases are written as  $\{\mathbf{A}_k\}_{k=1}^4$  and  $\{\mathbf{B}_k\}_{k=1}^4$ , respectively, and we suppose that their reference frames and measurements are aligned, i.e.,  $\mathbf{A}_k = \mathbf{B}_k$  for  $k = 1, 2, 3, 4$ . Assuming Alice and Bob are each operating in a four-dimensional Hilbert space with computational basis given by  $\mathbf{Z} = \{|i\rangle\}_{i=1}^4$ , their measurement bases are defined as  $\mathbf{A}_1 \equiv \mathbf{Z}$ ,  $\mathbf{A}_2 \equiv \{(|1\rangle \pm |2\rangle)/\sqrt{2}, (|3\rangle \pm |4\rangle)/\sqrt{2}\}$ ,  $\mathbf{A}_3 \equiv \{(|1\rangle \pm |3\rangle)/\sqrt{2}, (|2\rangle \pm |4\rangle)/\sqrt{2}\}$ , and  $\mathbf{A}_4 \equiv \{(|1\rangle + |2\rangle + |3\rangle - |4\rangle)/2, (|1\rangle + |2\rangle - |3\rangle + |4\rangle)/2, (|1\rangle - |2\rangle + |3\rangle + |4\rangle)/2, (|1\rangle - |2\rangle - |3\rangle - |4\rangle)/2\}$ , and similarly for Bob. It can be easily checked that bases 1 and 4 and bases 2 and 3 are mutually unbiased. Bases 1 and 2 are each chosen with probability  $p$ , while bases 3 and 4 are each chosen with probability  $q$ . Hence, we have that  $2p + 2q = 1$ , or  $q = 1/2 - p$ . When a measurement is made, Alice/Bob either observes a valid symbol or an outcome which is inconclusive. An example of the latter would be an empty detection event or a multiple detection event. Here, to overcome the problem of detection-loophole we assume that all successful detection events are independent of Alice/Bob's basis choices, and to overcome the issue of multiple detections, we simply assign a random symbol if a multiple detection event is observed. These conditions allow us to restrict the security analysis to post-selected joint states, which are the shared quantum states conditioned on both Alice and Bob receiving a valid symbol.

TABLE I: HEQKD Bases: All basis combinations in the HEQKD protocol and their effect on key generation. MUB = mutually-unbiased basis, and Bits/Photon, in this case, means bits of raw key per sifted coincident photon pair detected.

Alice Basis	Bob Basis	MUB?	Bits/Photon
1	1	N	2
1	2	N	1
1	3	N	1
1	4	Y	-
2	1	N	1
2	2	N	2
2	3	Y	-
2	4	N	1
3	1	N	1
3	2	Y	-
3	3	N	2
3	4	N	1
4	1	Y	-
4	2	N	1
4	3	N	1
4	4	N	2

After the measurement phase, Alice and Bob perform sifting (via public communication) to identify successful events according to their basis choices. We denote these sets by  $\mathcal{S}_{k,k'}$  and their respective lengths by  $m_{k,k'}$ . For example, the data belonging to set  $\mathcal{S}_{1,3}$  are the events in which Alice and Bob chose basis 1 and 3, respectively, and each detected one photon (though the results are not necessarily correct).

In our protocol, we extract secret keys from Alice's measurement data. We partition her data into four sets, namely, sets containing events in which Alice chooses either basis 1 or basis 2 (which data comprises the raw key) and sets containing events in which Alice chooses either basis 3 or basis 4 (used to determine Alice's QBER). Alice's data in basis 1 will be paired with Bob's data from basis 1, 2 and 3, and data in basis 2 will be paired with

Bob's data from basis 1, 2 and 4. Note that common bases should ideally generate perfectly correlated data (2 bits per measurement) while bases that are not mutually unbiased and common should ideally generate partially correlated data (1 bit per measurement).  $\mathcal{S}_{3,3}$  and  $\mathcal{S}_{4,4}$  are used for error estimation.  $\mathcal{S}_{3,4}$  and  $\mathcal{S}_{4,3}$  are unused. See Table I for the complete list of pairings.

We acknowledge there are others working on higher dimensional quantum key distribution[10–14]. To the best of our knowledge, no previous work has used hyperentanglement and been able to make the full set of measurements required to implement a higher dimensional quantum key distribution protocol with that hyperentangled state.

## EXPERIMENTAL SETUP

HEQKD like BBM92 requires the generation and distribution of entangled photons. As shown in Fig. 1, we prepare non-degenerate entangled photons at 1550 nm and 810 nm (see S.I. for more information) that are entangled in their polarization and time-bin degrees of freedom:

$$|\Psi_{AB}\rangle = \frac{1}{2}(|(Ht_1)_{810}(Ht_1)_{1550}\rangle + |(Vt_2)_{810}(Vt_2)_{1550}\rangle + |(Vt_1)_{810}(Vt_1)_{1550}\rangle + |(Ht_2)_{810}(Ht_2)_{1550}\rangle), \quad (2)$$

where  $|0\rangle \equiv |Ht_1\rangle$ ,  $|1\rangle \equiv |Vt_2\rangle$ ,  $|2\rangle \equiv |Vt_1\rangle$ , and  $|3\rangle \equiv |Ht_2\rangle$  for  $H$ ,  $V$ ,  $t_1$ , and  $t_2$  representing horizontal polarization, vertical polarization, time bin one, and time bin two, respectively. The measurements of the four bases are made using an analyzer interferometer, polarization optics, and a time-bin sorting circuit. The analyzer interferometer allows for measurements of superpositions of the time bins, while the polarization optics allow for measurements of different combinations of polarization and time bin. Measurements in bases 1 and 2 (or 3 and 4) are distinguished by the time-bin sorting circuit that is electrically in between the detectors and the time taggers; see S.I. for explanation of the necessity and operation of the time-bin sorting circuit. See S.I. Fig. 15 for a complete description of the mapping between the bases and measurements to the output time bins and detectors.

For our HEQKD, the probability of basis 1 and basis 2 is split evenly, as is the probability between basis 3 and basis 4, because of the 50/50 non-polarizing beamsplitters in Alice's and Bob's analyzers. However, the choice of measuring basis 1 or 2 *vs* basis 3 or 4 can

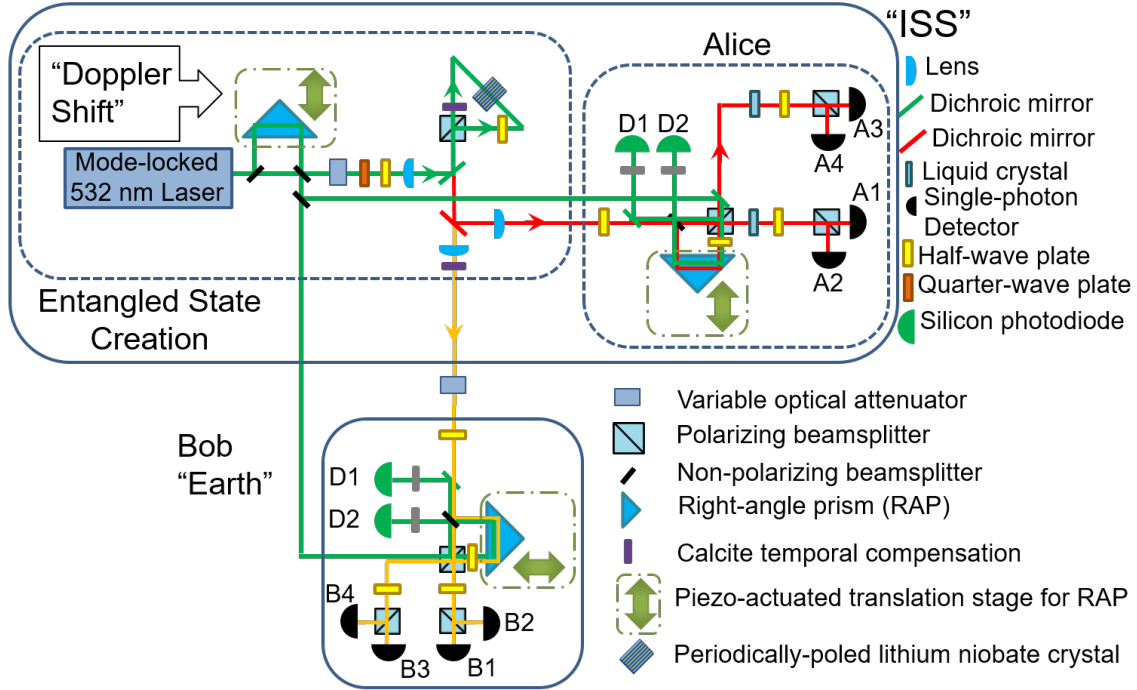


FIG. 1: BBM92 and HEQKD Optical Setup: Photonic ququarts entangled in polarization and time-bin are generated via spontaneous parametric downconversion in periodically-poled lithium niobate (See S.I.). Green lines are the 532-nm pump (and stabilization) beam; red and yellow are the signal (810 nm) and idler (1550 nm) photons, respectively. For BBM92, the pump right-angle prism was blocked so there was no time-bin entanglement. In the analyzer the short arm measured photons in the H/V basis and the long arm measured photons in the D/A basis; see S.I. for more information. For HEQKD, both time-bin and polarization entanglement are used; see S. I. Fig. 15 and S.I. Fig. 16 for the measurement-to-detector mapping. The phase in the phase-sensitive bases (bases 2, 3, and 4) is tuned by tilting the quarter waveplate before the Sagnac interferometer and/or actuating the liquid crystals after Alice’s analyzer interferometer. All half waveplates just before the detectors were set at  $22.5^\circ$  from horizontal. The half waveplate before the analyzer interferometer was set at  $0$  ( $22.5^\circ$ ) from horizontal for measurements in bases 1,2 (3,4).

be controlled by rotating a HWP at the front of the analyzer interferometer. For this experiment, we chose to measure in basis 1 and basis 2  $2p = 50\%$  of the time. Later in our analysis, we calculate the optimum value for this parameter in a space-to-ground

channel. Not randomly choosing the basis for every send attempt, i.e., every pump pulse, can lead to a vulnerability to photon-number-splitting attacks[15], e.g., in decoy-state QKD. However, entangled photons from SDPC are not susceptible to such attacks, because there is no correlation between photons of different pairs[16]. Since only detected pairs of photons make it into the raw key, we would only have to rotate the HWP at the average detected single-photon rate on the ground. At the rates we expect, this could be easily done by an electro-optic modulator.

## RESULTS

The intrinsic QBER of the system can be measured accurately for all bases when the probability of producing an entangled pair is low, so that the probability of producing multiple pairs (which can cause errors) is negligible. But since this also reduces the key rate, there is a trade-off, leading to an optimum pump power (pair production probability) that produces the most secret key per run, accounting for finite statistics. Fig. 2a shows the measured QBER vs pair production probability,  $P_p \sim \frac{S_A S_B}{RC_{AB}}$ , where  $S_i$  is the singles rates for Alice or Bob, R is the repetition rate of the laser, and  $C_{AB}$  is the total coincidence rate between Alice and Bob. See S.I. Fig 6-7 for a complete measured “crosstalk matrix” between Alice and Bob under normal operation, and when there is a simulated “intercept-resend attack” from Eve.

Since there would be a finite time window during orbit when we could establish the required line-of-sight quantum channel (see link analysis below), it was important to characterize the system for various values of channel transmission. Also, errors from detector noise and background events would start to dominate when the channel transmission becomes too low. Fig. 2b shows the measured QBER for each basis at decreasing values of channel transmission. At the highest measured transmission in Fig. 2b, our system (which was not optimized for key rate but QBER) produced  $\sim 2$ k sifted events/s. During those measurements, Alice’s channel transmission was fixed at -15 dB, the pair production probability was  $P_p = 0.015$ , and the laser repetition rate was 80 MHz.

By calculation, we found the optimum pair production probabilities,  $P_p$ , and basis choice probability,  $p$ , for our application to be about 0.12 and 0.2, respectively, as shown in Fig. 3a. In a direct comparison between HEQKD and BBM92, using a finite key analysis, we

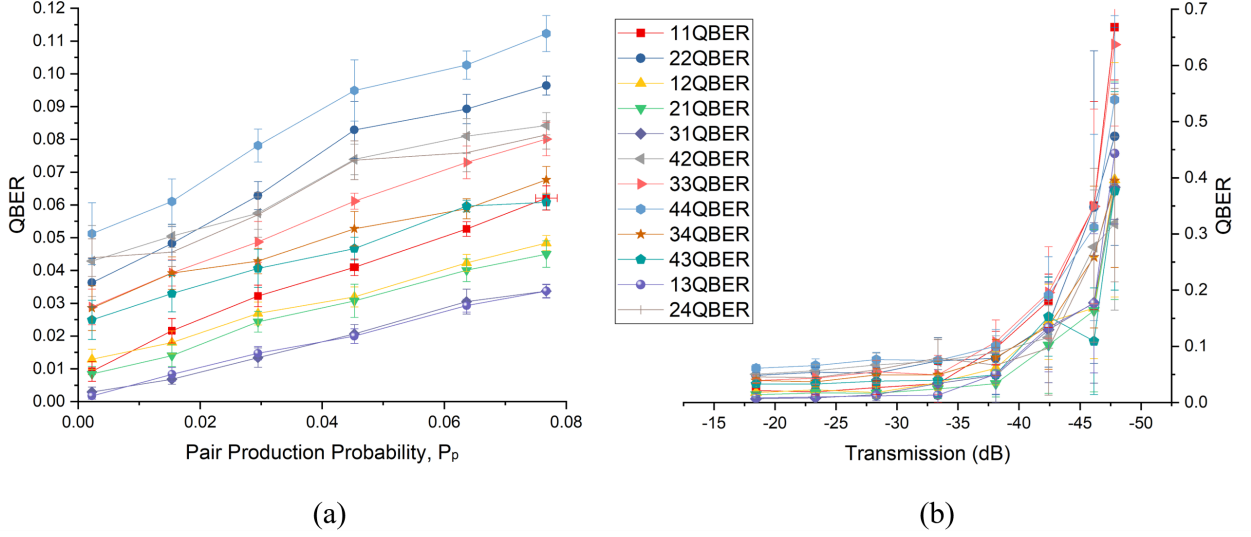


FIG. 2: QBER Characterization: Measurement of QBER for each key-generating HEQKD basis combination. (a) QBER measured as a function of pair production probability (adjusted by varying the pump laser power). The channel transmission for Alice and Bob are -15 dB and -18 dB, respectively. (b) QBER versus the transmission of the channel between the entangled photon source and Bob. During these measurements, Alice’s channel transmission was fixed at -15 dB and the pair production probability was  $P_p = 0.015$ .

found that HEQKD allows for secure key generation at higher losses than does BBM92, and for higher key rates than BBM92 when the losses are less extreme. This comparison was done with all system parameters being equal except choosing the optimum pair production probability of 0.12 for HEQKD and 0.04 for BBM92. See S.I. Table II for all system parameters used in the simulations. For use in the simulation, we also created  $\text{QBER}(P_p)$  for each basis combination using lines of best fit from the data in Fig. 2a. Fig. 3b, we calculated the secure key fraction for BBM92 and HEQKD; this is the fraction of bits from the raw key that make it in the secure key. Note, there is a larger than 10-dB span where only HEQKD provides a non-zero secure key fraction. This is primarily due to the increased error tolerance of higher dimensional protocols[17] in general, which allows for a higher pair production probability to be used.

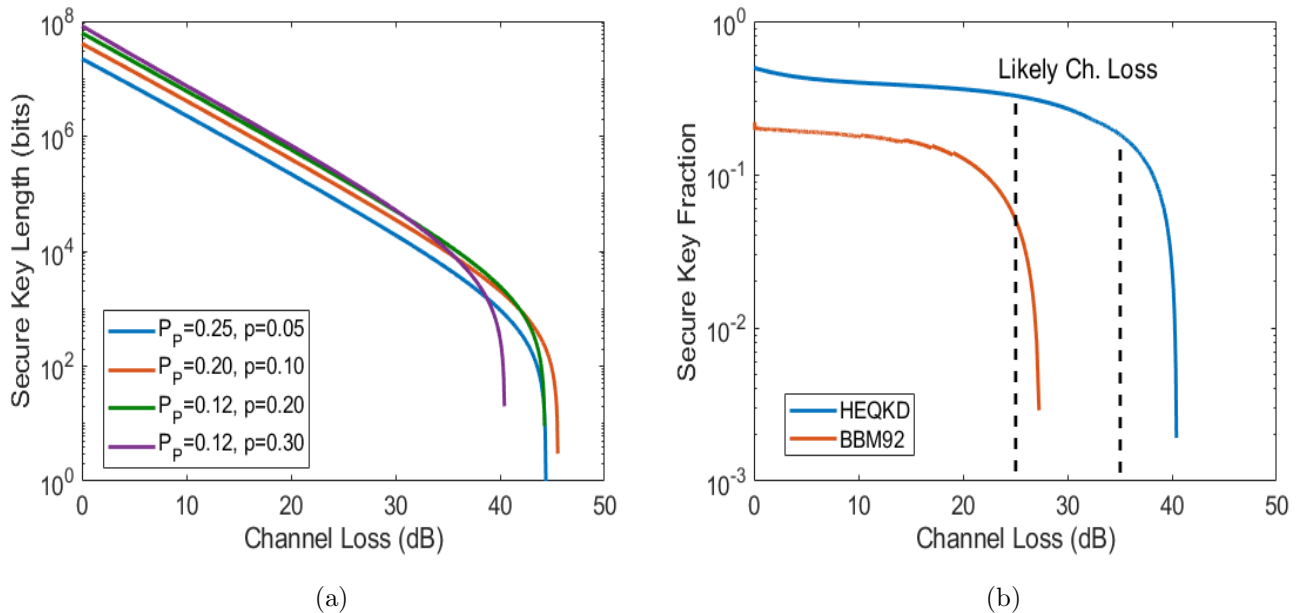


FIG. 3: Finite Key Simulations: (a) Calculated HEQKD secure key length vs Bob's channel loss for various pair production probabilities  $P_p$  and basis choice probability  $p$ , calculated using feasible future system parameters: 400-MHz laser repetition rate, 180-s orbital pass time,  $10^{-6}$  background noise, and Alice's total transmission = 0.3, including detection efficiency. See S.I. Table II for more details. (b) Calculated secure key fraction comparison between HEQKD and BBM92, choosing the optimum pair production probability of 0.12 for HEQKD and 0.04 for BBM92, with all other system parameters being equal. A likely range of channel loss ranges between 25 and 35 dB as indicated by the dashed lines.

### Link Analysis

The elevation-angle of the ISS with respect to some terrestrial observatory (say with a latitude of  $39^\circ$  N) changes as it passes overhead and has a maximum elevation angle that varies from pass to pass. With that in mind, displayed in Fig. 4, we show the predicted secure key length for HEQKD and BBM92, versus maximum elevation angle per pass, assuming the minimum acceptable elevation angle during a pass is  $20^\circ$  (below this we assume a reliable link cannot be established).

For these calculations, we used simulated orbit data for all orbital parameters. The simu-

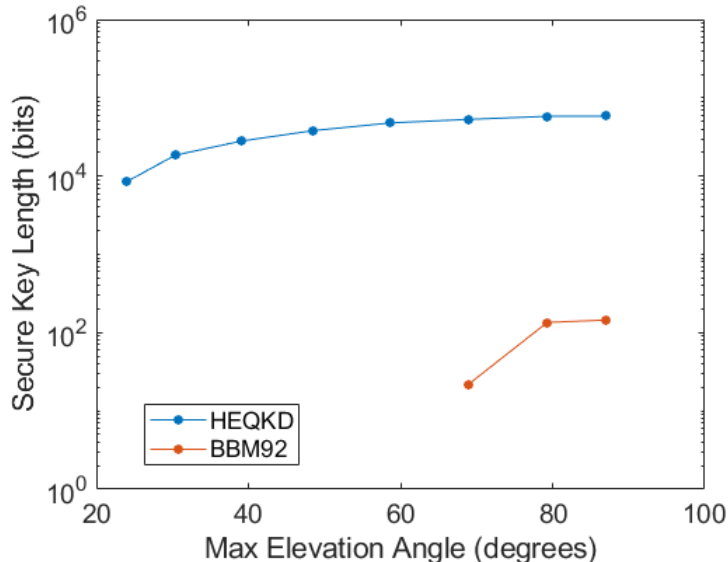


FIG. 4: Finite Key Link Analysis: Simulated secure key length per orbital pass for HEQKD and BBM92 vs the maximum elevation angle per orbital pass. The channel loss varied between 28 dB and 36 dB in this simulation. The pass time increases with the maximum elevation angle so higher elevation angle passes had more time to generate raw key. Simulations using feasible future system parameters: 400-MHz laser repetition rate, 180-s orbital pass time,  $10^{-6}$  background noise, and Alice’s total transmission = 0.3, including detection efficiency. See S.I. Table II and Link analysis section in S.I. for more details.

lation of the ISS orbit used a 400-km altitude and  $51^\circ$  inclination. The range was calculated from the ISS to a ground station located at  $39^\circ$  N latitude. We used the Friis equation to estimate channel transmission ( $\eta$ ) as a function of range ( $r$ )  $\eta(r) = (\pi D_T D_R / (4\lambda r))^2$  [18, 19], discretely integrated over the whole pass (for transmitting telescope diameter  $D_T = 0.1$  m, receiving telescope diameter  $D_R = 1$  m, and wavelength  $\lambda = 1550$  nm, with the added assumptions of a 6-dB loss for receiver telescope and adaptive optics efficiency and 4-dB loss from the analysis/detection system, and used the assumed system parameters in Table II.

Therefore, with those assumptions, a future implementation of this system in space should generate a secure key of substantial length in a single pass where, for most passes, BBM92 would not generate a secure key at all under the same operating conditions. This is because the maximum elevation angle and pass frequency are inversely proportional (passes with lower max elevation angle are more frequent).

TABLE II: System Parameters: Current and expected future system parameters relevant to simulation.

	Current System	Simulated System
Laser Repetition Rate	80 MHz	400 MHz
Pass Time	-	180 s
Detector Efficiency A	0.45	0.6
Detector Efficiency B	0.4	0.9
Measurement System Transmission	0.6	0.7
Heralding Efficiency	0.15	0.7
Background Noise	1.00E-05	1.00E-06

Finally, since any transmitter in space will be moving rapidly, the interval between adjacent time bins in the ground station’s reference frame initially will be reduced with respect to time-bin interval measured in the transmitter’s reference frame, as the transmitter is approaching. The intervals will match as the transmitter passes overhead, and as it moves away, the received interval will be longer. S.I. Fig. 17b shows a pictorial representation of this phenomena. Because the International Space Station (ISS), travels at about 7.7 km/s, the change in path length between two time bins separated by  $\sim 1$  ns is about  $20 \mu\text{m}$  for a pass directly overhead, which is over 80 radians for a wavelength of 1550 nm. To keep this Doppler shift (and any other time-varying phase shifts) from adversely affecting the protocol’s performance, we developed a phase stabilization system that uses a classical laser beam and proportional-integral feedback to track the path-length difference of the ground interferometer so it matches that of the emitted time bins throughout the pass (see S.I. for more information). With phase stabilization off, QKD is not possible because the QBER in some bases is too high, as seen in Fig. 5a; even though other bases are unaffected by the Doppler shift since their basis states, e.g., polarization, are time-bin phase insensitive. Fig. 5b shows the performance of HEQKD while a lab-simulated Doppler shift was occurring, with the phase stabilization activated. During the Doppler shift the QBER was held stable to  $< 1\%$  standard deviation.

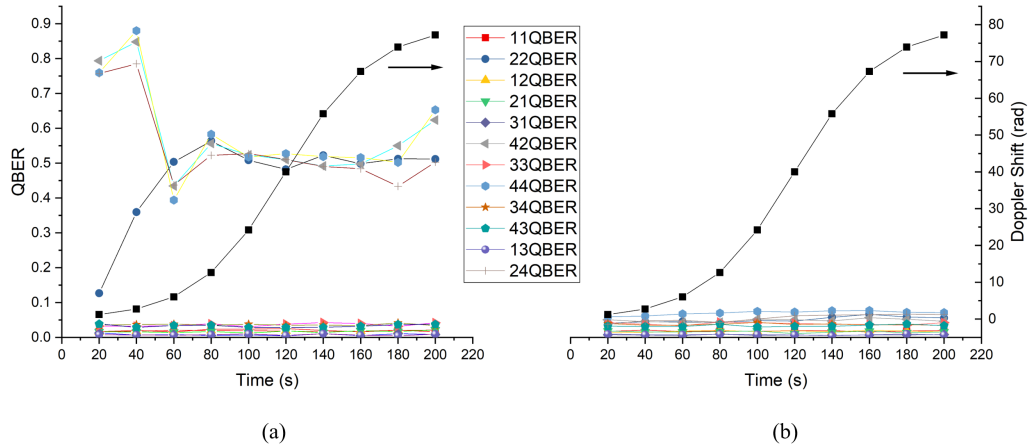


FIG. 5: Doppler Shift Effect on HEQKD: Measured QBER for all basis combinations during an in-lab simulated Doppler shift. (a) without phase stabilization. (b) with phase stabilization active.

## DISCUSSION

In Fig. 2a, we see significant variation in the intrinsic QBER of each basis, originating from the different physical processes that are present in the states and projections measured in each basis. QBER in basis 1 is only affected by imperfect H/V basis alignment between Alice and Bob and imperfect polarizing beamsplitter extinction ratio, leading to only  $\sim 1\%$  QBER ( $|HV\rangle$ -type terms in our state generation could also cause this same QBER, but are apparently negligible, since the basis 1 QBER matches our classical measurements of the basis alignment and polarizing beamsplitter). Basis 2 is affected by the same influences as basis 1, but is also affected by the temporal entanglement visibility ( $\sim 96\% \rightarrow 2\%$  QBER) and imbalances in the measured amplitudes of the terms in the superposition ( $\sim 0.5\%$  QBER). Basis 3 is also affected by the same error processes as basis 1, and is also affected by imperfect polarization entanglement purity of the source (D/A visibility  $\sim 98\% \rightarrow 1\%$  QBER) and imbalances in the measured amplitudes of the terms in the superposition ( $\sim 0.5\%$  QBER). Finally, basis 4 is affected by all previously mentioned error processes, and thus has the highest total QBER.

From these measurements and analyses, we find this system suitable for operation in the channel between space and earth. Furthermore, we find that the use of time-bin qubits in

general should be feasible for a channel that includes an orbiting platform, assuming one compensates for the adverse effect from the Doppler shift, as we have done. To successfully execute this protocol in a space-to-earth channel, active polarization compensation (to correct for rotations produced by the sending and receiving optics) and phase stabilization (to phase stabilize the time bins from the Doppler shift and from other variations, e.g., satellite vibrations or laboratory temperature fluctuations) must be implemented in real time. Additionally, after the previous compensation systems have been activated, but prior to protocol execution, a phase calibration step is necessary for bases which include superpositions of time bins, so that Alice and Bob are indeed measuring in the same bases. Implementing such systems is readily achievable with current technology.

### ACKNOWLEDGMENTS

Thanks to Michael Wayne and Kristina Meier for discussions regarding design of the time-bin sorting circuit, and to Chris Chopp for assistance in prototyping and PCB layout of the time-bin sorting circuit. Thanks to MIT-Lincoln Laboratory for the orbital simulation calculations. J.C.C and P.G.K acknowledge support from NASA Grant No. NNX13AP35A and NASA Grant No. NNX16AM26G. J.C.C acknowledges support from a DoD, Office of Naval Research, National Defense Science and Engineering Graduate Fellowship (NDSEG). C.C.W.L. acknowledges support from NUS startup grant R-263-000-C78-133/731 and CQT fellow grant.

---

\* jchapmn2@illinois.edu

- [1] R. J. Hughes *et al.*, IEEE Aerospace Conf. Proc. (2000).
- [2] M. Aspelmeyer, T. Jennewein, M. Pfennigbauer, W. R. Leeb, and A. Zeilinger, IEEE Journal of Selected Topics in Quantum Electronics **9**, 1541 (2003).
- [3] J. Yin *et al.*, Science **356**, 1140 (2017).
- [4] S.-K. Liao *et al.*, Nature **549**, 43 (2017).
- [5] J. A. Grieve, R. Bedington, Z. Tang, R. C. Chandrasekara, and A. Ling, Acta Astronautica **151**, 103 (2018).

- [6] G. Vallone, D. Bacco, D. Dequal, S. Gaiarin, V. Luceri, G. Bianco, and P. Villoresi, *Physical Review Letters* **115**, 040502 (2015).
- [7] C. J. Pugh, S. Kaiser, J.-P. Bourgoïn, J. Jin, N. Sultana, S. Agne, E. Anisimova, V. Makarov, E. Choi, B. L. Higgins, *et al.*, *Quantum Science and Technology* **2**, 024009 (2017).
- [8] F. Steinlechner, S. Ecker, M. Fink, B. Liu, J. Bavaresco, M. Huber, T. Scheidl, and R. Ursin, *Nature communications* **8**, 15971 (2017).
- [9] C. H. Bennett, G. Brassard, and D. Mermin, *N.*, *Phys. Rev. Lett.* **68**, 557 (1992).
- [10] N. T. Islam, C. C. W. Lim, C. Cahall, J. Kim, and D. J. Gauthier, *Science advances* **3**, e1701491 (2017).
- [11] S. Ecker, F. Steinlechner, M. Fink, B. Liu, J. Bavaresco, M. Huber, T. Scheidl, and R. Ursin, in *Proc. SPIE 10799*, Vol. 10799 (2018).
- [12] Z. Zhang, J. Mower, D. Englund, F. N. Wong, and J. H. Shapiro, *Physical review letters* **112**, 120506 (2014).
- [13] M. Mirhosseini, O. S. Magaña-Loaiza, M. N. OSullivan, B. Rodenburg, M. Malik, M. P. Lavery, M. J. Padgett, D. J. Gauthier, and R. W. Boyd, *New Journal of Physics* **17**, 033033 (2015).
- [14] F. Bouchard, K. Heshami, D. England, R. Fickler, R. W. Boyd, B.-G. Englert, L. L. Sánchez-Soto, and E. Karimi, *arXiv preprint arXiv:1802.05773* (2018).
- [15] N. Lütkenhaus, *Physical Review A* **61**, 052304 (2000).
- [16] S. Bettelli, T. Lorünser, M. Peev, E. Querasser, M. Dušek, L. Bartůšková, B. Blauensteiner, H. Huebel, A. Poppe, and A. Zeilinger, in *The European Conference on Lasers and Electro-Optics* (Optical Society of America, 2007) p. JSI2.2.
- [17] N. J. Cerf, M. Bourennane, A. Karlsson, and N. Gisin, *Phys. Rev. Let.* **88**, 127902 (2002).
- [18] H. T. Friis, *IEEE spectrum* **8**, 55 (1971).
- [19] S. B. Alexander, *Optical communication receiver design* (SPIE Optical engineering press, Bellingham, Washington, USA, 1997).
- [20] M. Tomamichel, C. C. W. Lim, N. Gisan, and R. Renner, *Nat. commun.* **3** (2012).
- [21] J. Mueller-Quade and R. Renner, *New J. of Phys.* **11** (2009).
- [22] M. Tomamichel and M. Hayashi, *IEEE Trans. on Inf. Theory* **59**, 7693 (2013).
- [23] R. Koenig, R. Renner, and C. Schaffner, *IEEE Trans. on Inf. Theory* **55**, 4337 (2009).
- [24] B. S. Shi and A. Tomita, *Phys. Rev. A* **69**, 013803 (2004).
- [25] T. Kim, M. Fiorentino, and F. N. Wong, *Phys. Rev. A* **73**, 012316 (2006).

- [26] K. Zielnicki *et al.*, J. Mod. Opt. **65**, 1141 (2018).
- [27] T. M. Graham, *Using Hyperentanglement for advanced quantum communication*, Ph.D. thesis, University of Illinois at Urbana-Champaign (2016).
- [28] F. Marsili *et al.*, Nat. Phot. **7**, 210 (2013).
- [29] N. Minorsky, J. Amer. Soc. Naval Eng. **34**, 280 (1922).
- [30] A. Einstein, Annalen der Physik **322**, 891 (1905).

## SUPPLEMENTAL INFORMATION

### HEQKD and BBM92 Finite Key Analysis

#### *Preliminaries: models*

In the following, we will analyze the finite-key security of entanglement-based BB84 (also called BBM92) and a high-dimensional QKD protocol using two sets of two mutually unbiased bases. The security proof technique that we will be using is the entropic uncertainty relation, which is based on Ref. [20].

In both of the above protocols, we assume that entanglement is generated in Alice's laboratory using a practical light source, namely via a spontaneous parametric down-conversion (SPDC) source, where a non-linear crystal is used to split a strong laser beam into pairs of correlated photons. Quantum mechanically, we can write the output state (using vector representation) of such a source as

$$|\Psi\rangle_{AB} \equiv \cosh^{-2}(\chi) \sum_{n=0}^{\infty} \sqrt{n+1} \tanh^n(\chi) |\psi_n\rangle_{AB}, \quad (3)$$

where

$$|\psi_n\rangle_{AB} \equiv \frac{1}{n+1} \sum_{k=0}^n (-1)^k |n-k, k\rangle_A \otimes |k, n-k\rangle_B. \quad (4)$$

Accordingly, the probability to get an  $n$ -photon pair is

$$P_n \equiv \frac{(n+1)\gamma^n}{(1+\gamma)^{n+2}}, \quad (5)$$

where  $\gamma \equiv \sinh^2(\chi)$  is related to the pump power of the laser, and  $P_1=P_p$ , the pair production probability, mentioned elsewhere in this work.

For our purpose we only need to know the photon number distribution of the SPDC source. Unlike the prepare-and-measure scenario, multi-photon pairs in the entanglement-based scenario are robust against basis-dependent and loss-dependent attacks (e.g., photon-number-splitting attacks), due to the fact that each pair in a multi-pair pulse is independent, and Alice's and Bob's measurements act independently on each received photon.

To model the detection rates (which are needed for the simulation), we define  $\eta_A$  and  $\eta_B$  to be the overall detection efficiencies for Alice and Bob, respectively. Note that  $\eta_A$  and  $\eta_B$  include all the losses due to the quantum channel, coupling loss, and detection inefficiency. Using this definition, it is easy to see that the probability of observing a coincident detection (i.e., at least a click on each side) given the emission of an  $n$ -photon pair,  $|\psi_n\rangle$ , is

$$\eta_n = [1 - (1 - \eta_A)^n][1 - (1 - \eta_B)^n]. \quad (6)$$

In addition, we define the *yield* of an  $n$ -photon pair to be  $Y_n$ , which is the conditional probability that a coincident detection is observed given the source emits an  $n$ -photon pair. We may further model the  $n$ -photon yield as

$$Y_n = [1 - (1 - \xi_A)(1 - \eta_A)^n][1 - (1 - \xi_B)(1 - \eta_B)^n], \quad (7)$$

where  $\xi_A$  ( $\xi_B$ ) is the probability of observing a dark detection on Alice's (Bob's) side. Therefore, in the case of zero photon emission, we have

$$Y_0 = \xi_A \xi_B. \quad (8)$$

Using the above models, the overall detection rate for a given  $\gamma$  is

$$R_\gamma = \sum_{n=0}^{\infty} P_n Y_n = 1 - \frac{1 - \xi_A}{(1 + \eta_A \gamma)^2} - \frac{1 - \xi_B}{(1 + \eta_B \gamma)^2} + \frac{(1 - \xi_A)(1 - \xi_B)}{(1 + \eta_A \gamma + \eta_B \gamma - \eta_A \eta_B \gamma)^2}. \quad (9)$$

The overall (expected) quantum bit error rate (QBER) is given as

$$Q_\gamma^{2D} R_\gamma = V_\gamma = \frac{R_\gamma}{2} - \frac{2(1/2 - \delta)\eta_A \eta_B \gamma (1 + \gamma)}{(1 + \eta_A \gamma)(1 + \eta_B \gamma)(1 + \eta_A \gamma + \eta_B \gamma - \eta_A \eta_B \gamma)} \quad \text{and} \quad (10)$$

$$Q_\gamma^{4D} R_\gamma = V_\gamma = \frac{3R_\gamma}{4} - \frac{2(3/4 - \delta)\eta_A \eta_B \gamma (1 + \gamma)}{(1 + \eta_A \gamma)(1 + \eta_B \gamma)(1 + \eta_A \gamma + \eta_B \gamma - \eta_A \eta_B \gamma)}, \quad (11)$$

where  $\delta$  is the intrinsic QBER of the quantum channel connecting Alice and Bob. Here  $Q_\gamma^{2D}$  ( $Q_\gamma^{4D}$ ) is the QBER for BBM92 (HEQKD).

*Security Bound for BBM92*

Having defined the quantum channel and source models, we are now ready to derive a bound on the extractable key length (denoted by  $\ell$ ) for a given *post-processing block size* (the number of raw bits we collect in one execution of the protocol).

To further model the security of the QKD protocol, we consider a ( $d = 2$ ) QKD protocol with two mutually unbiased bases. The bases are uniformly chosen (with  $1/2$  probability each) and the raw key is generated from both bases. That is, the raw key is randomly sampled from the measurement data (of size  $N$ ); thus the size of the raw key is fixed to some positive integer  $n$ . Following standard security definitions [21], we say that the QKD protocol is  $\varepsilon$ -secure if it is both  $\varepsilon_{\text{sec}}$ -secret and  $\varepsilon_{\text{cor}}$ -correct. For the first condition, the protocol is called  $\varepsilon_{\text{sec}}$ -secret if the joint state of the output secret key (say on Alice side) and the adversary's total quantum information is statistically indistinguishable from the ideal output state except with some small probability  $\varepsilon_{\text{sec}}$ . The ideal output state is an output key which is uniformly random (in the key space) and completely independent of the adversary's total information. For the second condition, the protocol is called  $\varepsilon_{\text{cor}}$ -correct if the output secret keys on Alice and Bob's sides are identical except with some small probability  $\varepsilon_{\text{cor}}$ .

The starting point of our security analysis is to ask how many secret bits can be extracted from Alice' raw key  $X$  (of size  $n$ ) given  $E$  (Eve' total information about the QKD system). To this end, we use the quantum leftover-hash lemma [22] to bound the secret key length,  $\ell$ , giving

$$\ell = \max_{\beta \in (0, \varepsilon_{\text{sec}}/2]} \left\lfloor H_{\min}^{\varepsilon_{\text{sec}}/2-\beta}(X|E) + 4 \log_2 \beta - 2 \right\rfloor, \quad (12)$$

where the left-hand term in the floor function is the smooth min-entropy of  $X$  given  $E$  (see Ref. [23] for more details).

Using the fact that there exists a squashing model for two mutually unbiased measurements (it applies regardless of whether the implementation is active or passive basis choice), we can bound the min-entropy using the entropic uncertainty relation [20], assuming the measurements on Alice's side are mutually unbiased (e.g., no polarization misalignment at the measurement level). More specifically, we have

$$H_{\min}^{\varepsilon_{\text{sec}}/2-\beta}(X|E) \geq n(1 - h_2(Q_{\text{obs}}^{2D} + \Delta)) - \text{Synd}_{\text{EC}}^{2D} - \log_2 \frac{2}{\varepsilon_{\text{cor}}} \quad \text{and} \quad (13)$$

$$\text{Synd}_{\text{EC}}^{2D} = 1.12nh_2(Q_{\text{obs}}^{2D}), \quad (14)$$

where

$$\Delta \equiv \sqrt{\frac{n+k}{nk} \frac{k+1}{k} \log \frac{1}{\beta}}, \quad (15)$$

and  $\text{Synd}_{\text{EC}}^{2D}$  and  $\log_2 2/\varepsilon_{\text{cor}}$  are the leakages due to error correction and verification, respectively. Putting everything together, we get

$$\ell^{2D} = \max_{\beta \in (0, \varepsilon_{\text{sec}}/4)} \left[ n(1 - h_2(Q_{\text{obs}}^{2D} + \Delta)) - \text{Synd}_{\text{EC}}^{2D} - \log_2 \frac{8}{\beta^4 \varepsilon_{\text{cor}}} \right]. \quad (16)$$

### *Security Bound for HEQKD*

To compute the finite-key security of Alice' data, we first need to introduce some random variables to capture the random behavior of the measurements. To that end, let  $\mathbf{X}_1$  be the random string of length  $n_1 = m_{1,1} + m_{1,2} + m_{1,3}$  describing Alice' measurement outcomes when she chooses basis 1. Likewise, for the case when Alice chooses basis 2 we write  $\mathbf{X}_2$  to denote the random string of  $n_2 = m_{2,1} + m_{2,2} + m_{2,4}$ . Recall, the lengths of the sifted events when Alice measures in basis  $k$  and Bob measures in basis  $k'$  are denoted by  $m_{k,k'}$ . Our immediate goal now is to show that it is possible to extract a secret key of length  $\ell > 0$  from  $\mathbf{X}_1 \mathbf{X}_2$  if certain experimental conditions are met.

The starting point of our security analysis is to ask how many secret bits can be extracted from Alice' raw key  $\mathbf{X}$  (of size  $n$ ) given  $\mathbf{E}^+$  (Eve's total information about the overall joint state shared between Alice and Bob, including the classical communication sent by Alice to Bob). To this end, we use the quantum leftover-hash lemma [22] to determine the secret key length,  $\ell$ , giving

$$\ell = \max_{\beta \in (0, \varepsilon_{\text{sec}}/2]} \left\lfloor H_{\min}^{\varepsilon_{\text{sec}}/2-\beta}(\mathbf{X}_1 \mathbf{X}_2 | \mathbf{E}^+) + 4 \log_2 \beta - 2 \right\rfloor, \quad (17)$$

where the left-hand term in the floor function is the smooth min-entropy of  $\mathbf{X}_1 \mathbf{X}_2$  given  $\mathbf{E}^+$  (see Ref. [23] for more details). We can further break up the min-entropy term into two parts by using a chain-rule inequality for smooth min-entropies,

$$H_{\min}^{\varepsilon_{\text{sec}}/2-\beta}(\mathbf{X}_1 \mathbf{X}_2 | \mathbf{E}^+) \geq H_{\min}^{\bar{\varepsilon}}(\mathbf{X}_1 | \mathbf{X}_2 \mathbf{E}^+) + H_{\min}^{\bar{\varepsilon}}(\mathbf{X}_2 | \mathbf{E}^+) + \log(1 - (1 - \bar{\varepsilon}^2)^{1/2}), \quad (18)$$

where  $\bar{\varepsilon} = \varepsilon_{\text{sec}}/6 - \beta/3$ . To further simplify the analysis, we assume that  $\mathbf{X}_1$  and  $\mathbf{X}_2$  are independent. In the experiment, this assumption can be achieved by having Alice prepare highly entangled photon pairs (independent pairs), measure one half of each entangled photon pair, and send the other half to Bob via the quantum channel. This procedure in effect

produces random outcomes in each run, which implies  $\mathbf{X}_1$  and  $\mathbf{X}_2$  are independent variables. With this, we have that

$$H_{\min}^{\varepsilon_{\text{sec}}/2-\beta}(\mathbf{X}_1\mathbf{X}_2|\mathbf{E}^+) \geq H_{\min}^{\bar{\varepsilon}}(\mathbf{X}_1|\mathbf{E}^+) + H_{\min}^{\bar{\varepsilon}}(\mathbf{X}_2|\mathbf{E}^+) + \log(1 - (1 - \bar{\varepsilon}^2)^{1/2}), \quad (19)$$

where now the smooth entropy terms  $H_{\min}^{\bar{\varepsilon}}(\mathbf{X}_1|\mathbf{E}^+)$  and  $H_{\min}^{\bar{\varepsilon}}(\mathbf{X}_2|\mathbf{E}^+)$  can be treated independently. To translate these terms into expressions that can be bounded using experimental data, we use a version of entropic uncertainty relations for two  $d = 4$  mutually unbiased bases to get

$$H_{\min}^{\bar{\varepsilon}}(\mathbf{X}_1|\mathbf{E}^+) \geq 2n_1 - H_{\max}^{\bar{\varepsilon}}(\mathbf{T}_1|\mathbf{T}'_1), \quad (20)$$

$$H_{\min}^{\bar{\varepsilon}}(\mathbf{X}_2|\mathbf{E}^+) \geq 2n_2 - H_{\max}^{\bar{\varepsilon}}(\mathbf{T}_2|\mathbf{T}'_2), \quad (21)$$

where  $\mathbf{T}_1$  and  $\mathbf{T}'_1$  are Alice's and Bob's measurement outcomes corresponding to basis 4, and  $\mathbf{T}_2$  and  $\mathbf{T}'_2$  are the measurement outcomes corresponding to basis 3. Here, we suppose that the measurements are acting locally on a four-dimensional Hilbert space, which is a reasonable assumption since in practice Alice' light source produces independent entangled photon pairs. Assuming the error probabilities of Alice and Bob, within a basis, are uniformly distributed (i.e., they can be modelled by a depolarizing channel), then we have that

$$H_{\min}^{\bar{\varepsilon}}(\mathbf{X}_1|\mathbf{E}^+) \geq n_1(2 - h_4(Q_{4,4}^{4D} + \nu(n_1, m_{4,4}, \bar{\varepsilon}))), \quad (22)$$

$$H_{\min}^{\bar{\varepsilon}}(\mathbf{X}_2|\mathbf{E}^+) \geq n_2(2 - h_4(Q_{3,3}^{4D} + \nu(n_2, m_{3,3}, \bar{\varepsilon}))), \quad (23)$$

where  $Q_{k,k'}^{4D}$  is the observed error rate conditioned on Alice and Bob choosing basis  $k$  and  $k'$ , and

$$\nu(n, k, \varepsilon) = \sqrt{\frac{(n+k)(k+1)\log(2/\varepsilon)}{nk^2}}, \quad (24)$$

is the statistical error due to finite sampling. Note that in the infinite key limit this term goes to zero.

Now, putting everything together, we can establish a lower bound on  $H_{\min}^{\varepsilon_{\text{sec}}/2-\beta}(\mathbf{X}_1\mathbf{X}_2|\mathbf{E}^+) \geq n_{\text{ext}}$ :

$$n_{\text{ext}} \equiv n_1(2 - h_4(Q_{4,4}^{4D} + \nu(n_1, m_{4,4}, \bar{\varepsilon}))) + n_2(2 - h_4(Q_{3,3}^{4D} + \nu(n_2, m_{3,3}, \bar{\varepsilon}))) - \text{Synd}_{\text{EC}}^{4D} - \log_2 \frac{2}{\varepsilon_{\text{cor}}}, \quad (25)$$

$$\begin{aligned} \text{Synd}_{\text{EC}}^{4D} = & 1.2n_1h_4(\min[0.75, p^2Q_{1,1}^{4D} + p^2Q_{1,2}^{4D} + pqQ_{1,3}^{4D}]) + \\ & 1.2n_2h_4(\min[0.75, p^2Q_{2,1}^{4D} + p^2Q_{2,2}^{4D} + pqQ_{2,4}^{4D}]), \end{aligned} \quad (26)$$

where  $\text{Synd}_{\text{EC}}^{4D}$  and  $\log_2 2/\varepsilon_{\text{cor}}$  are the leakages due to error correction and verification, respectively. Finally, we then get

$$\ell^{4D} = \max_{\beta \in (0, \varepsilon_{\text{sec}}/4)} [n_{\text{ext}} + 4 \log_2 \beta - 2]. \quad (27)$$

### HEQKD Crosstalk Matrix and Eavesdropping Measurement

S.I. Fig. 6 shows the ‘‘crosstalk matrix’’ for all bases in the HEQKD protocol, demonstrating that those bases can operate at low QBER in our system. In order to verify the ability of HEQKD to detect an eavesdropper, we inserted in the channel to Bob a 9-mm thick, a-cut calcite crystal oriented so that H and V polarizations are unaltered but travel at different speeds. The calcite is thick enough so the H and V polarizations can no longer interfere after exiting the calcite, because their wavepackets no longer overlap temporally. The calcite introduces a  $\sim 5$ -ps relative delay, much larger than  $\sim 1.7$ -ps coherence time of the 1.5-nm (0.4-nm) bandwidth 1550-nm (810-nm) photons. This simulates an eavesdropper that measures only in basis 1 and simply records, then resends to Bob, what is measured. With this technique, the eavesdropper gains a significant amount of information at the necessary cost of introducing a significant amount of errors. S.I. Fig. 7 shows the expected and measured results of the eavesdropping. As expected, the results show a greatly increased QBER in all bases involving measurements using superpositions of polarizations.

### Polarization-Entangled BBM92

As alluded to elsewhere in this work, our system also has the capability to execute the usual 2-state BBM92 protocol, in which Alice and Bob receive photons from a maximally entangled pair source. In our case, the photons are entangled in their polarization, and the state shared between Alice and Bob is

$$|\Psi_{AB}\rangle = \frac{1}{\sqrt{2}}|t_1t_1\rangle \otimes (|HH\rangle + |VV\rangle). \quad (28)$$

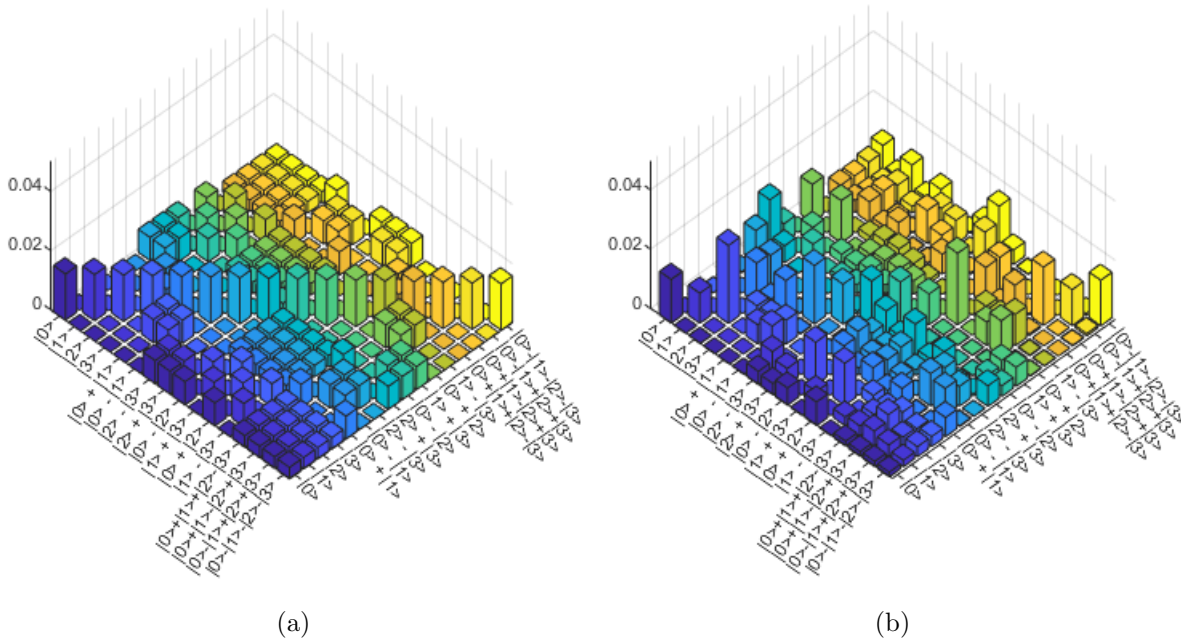


FIG. 6: HEQKD Crosstalk Matrix For All Bases: (a) Ideal normalized crosstalk matrix. Alice (Bob) is on the right (left) axis. (b) Measured normalized crosstalk matrix.

Alice and Bob, independently and randomly, measure in the two bases

$$\{|H\rangle, |V\rangle\} \text{ and } \{|D\rangle \equiv \frac{1}{\sqrt{2}}(|H\rangle + |V\rangle), |A\rangle \equiv \frac{1}{\sqrt{2}}(|H\rangle - |V\rangle)\}. \quad (29)$$

The basis for measurement is randomly chosen by the 50/50 non-polarizing first beamsplitter in Alice or Bob's delay interferometer. If the photon goes through the short path, it is analyzed in the H/V basis; if it travels the long path, it is analyzed in the D/A basis because of a half waveplate (HWP) that effectively rotates the basis of that beamsplitter port from H/V to D/A.

In addition to QBER, another useful metric is the shared information entropy, a.k.a., the mutual information per photon, which allows the user to know how many bits of key are transferred per photon after sifting (removing trials where Alice and Bob measured in different bases), in the asymptotic limit. The sifted shared entropy (SSE) is defined as:

$$S(A : B) \equiv S(A) + S(B) - S(A, B), \quad (30)$$

where,

$$S(X) \equiv - \sum_i p_i \log(p_i) \text{ and } S(X, Y) \equiv - \sum_{i,j} p_{i,j} \log(p_{i,j}). \quad (31)$$

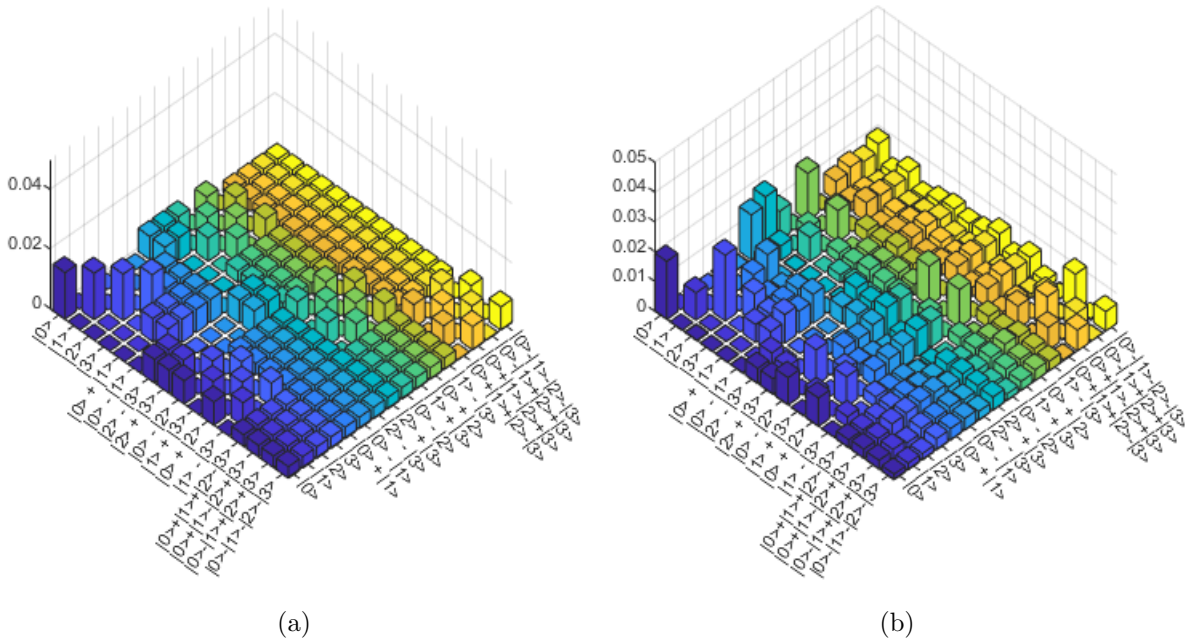


FIG. 7: HEQKD Crosstalk Matrix For All Bases With Eavesdropper: (a) Ideal HEQKD normalized crosstalk matrix when an eavesdropper performs an ideal intercept-resend attack on basis 1. Alice (Bob) is on the right (left) axis. (b) Measured HEQKD normalized crosstalk matrix with a 9-mm thick, a-cut calcite crystal which decoheres the polarization in the H/V basis. QBER per basis for measured (ideal) system:  $QBER_{11} = 0.02(0.00)$ ,  $QBER_{12} = 0.02(0.00)$ ,  $QBER_{13} = 0.01(0.00)$ ,  $QBER_{21} = 0.02(0.00)$ ,  $QBER_{22} = 0.52(0.50)$ ,  $QBER_{24} = 0.49(0.50)$ ,  $QBER_{31} = 0.01(0.00)$ ,  $QBER_{33} = 0.50(0.50)$ ,  $QBER_{34} = 0.50(0.50)$ ,  $QBER_{42} = 0.47(0.50)$ ,  $QBER_{43} = 0.50(0.50)$ , and  $QBER_{44} = 0.53(0.50)$ .

S.I. Fig. 8 shows the performance of our BBM92 setup. To test the ability of the system to detect an eavesdropper, we inserted in the channel to Bob a 9-mm thick, a-cut calcite crystal oriented so that H and V polarizations are unaltered but travel at different speeds. The calcite is thick enough so the H and V polarizations can no longer interfere after exiting the calcite, because their wavepackets no longer overlap temporally. This simulates an eavesdropper that measures only in the H/V basis and simply records, then resends to Bob, what is measured. With this technique, the eavesdropper gains a significant amount of information at the necessary cost of introducing a significant amount of errors. Results

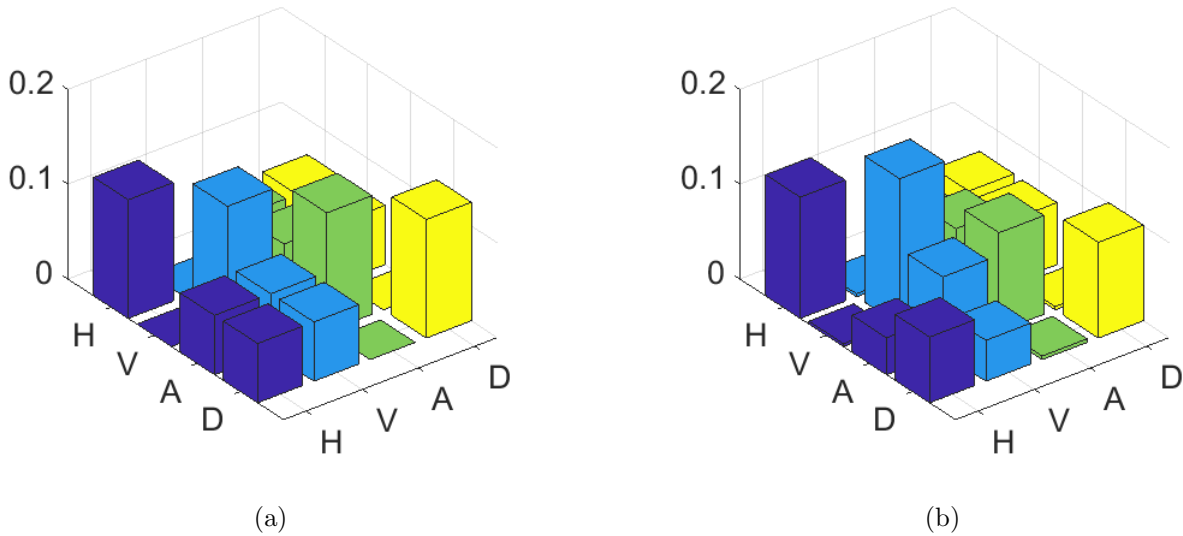


FIG. 8: BBM92 Crosstalk Matrix: (a) Ideal BBM92 normalized crosstalk matrix. H/V QBER = 0, D/A QBER = 0, and SSE = 1 bit. (b) Measured BBM92 normalized crosstalk matrix. H/V QBER = 0.009, D/A QBER = 0.019, and SSE H/V (D/A) = 0.92 (0.87) bits.

shown in S.I. Fig. 9 confirm that our system detects this increase in errors with the calcite in place. The right side indeed shows an increase in errors as evidenced by the large off-diagonal elements in the D/A basis sub-matrix.

Since there is a finite time window during orbit when we can establish the line-of-sight quantum channel, it is important to characterize the system for various values of channel transmission. Also, errors from detector noise and background events become significant when the channel transmission becomes too low. S.I. Fig. 10 shows the results of a measurement where the QBER is recorded for each basis at decreasing values of channel transmission. At the highest measured transmission in S.I. Fig. 10, our system (which was not optimized for key rate but QBER) produced  $\sim 2\text{k}$  sifted events/s. During those measurements, Alice's channel transmission was fixed at  $-15$  dB, the pair production probability was  $P_p = 0.025$ , and the laser repetition rate was  $80$  MHz. We conclude that, with our current background and detector noise (which are comparable to what is expected in an actual implementation), the system can operate at reasonably low QBER ( $< 0.05$ ) until about  $-35$  dB of channel transmission (corresponding to a transmission of  $0.32\%$ ), neglecting finite statistics. Using a finite key estimation technique, we see in S.I. Fig 12 that the minimum allowed chan-

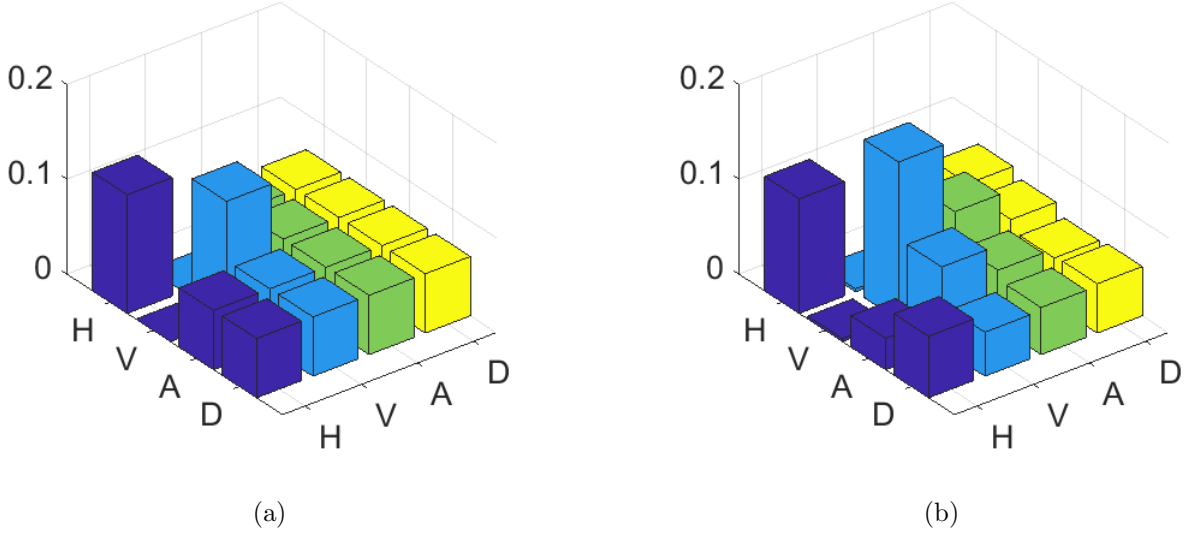


FIG. 9: BBM92 Eavesdropping Crosstalk Matrix: (a) Ideal BBM92 normalized crosstalk matrix when an eavesdropper measures the polarization qubit in the H/V basis. H/V QBER = 0, D/A QBER = 0.5, and SSE H/V (D/A) = 1 (0) bits. (b) Measured BBM92 normalized crosstalk matrix with a calcite crystal which decoheres the polarization in the H/V basis, simulating an eavesdropper performing a quantum measurement in the H/V basis. H/V QBER = 0.028, D/A QBER = 0.48, and SSE H/V (D/A) = 0.83 (0.002) bits.

nel transmission is about -28 dB, in agreement with our rough estimate from measurement above. Additionally, to quantify the errors associated with undesirable simultaneous generation of multiple pairs from the entangled photon source, we measured the QBER as a function of pair production probability, the probability that a pair is produced in a given pump laser pulse; the results from that measurement are in S.I. Fig. 11. In S.I. Fig. 12 we find, when accounting for finite statistics, the optimum  $P_p$  for an implementation of this protocol from the ISS to Earth is  $P_p = 0.04$ .

### State Generation and Detection

To generate entangled photons in time-bin and polarization, we use an 80-MHz mode-locked, 532-nm laser, frequency doubled from 1064 nm, with a pulse width  $\sim 7$  ps (Spectra Physics Vanguard 2.5W 355 laser). Each pulse of this beam is split into two time-bins using a  $\sim 2.4$ -ns delay (see Fig. 1). The beam is then used to pump a type-0 periodically-

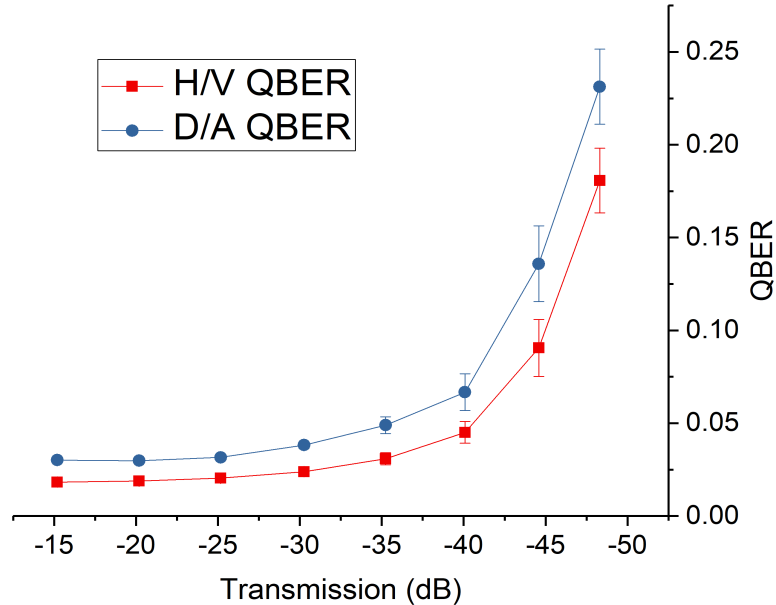


FIG. 10: BBM92 QBER vs Transmission: Measurement of QBER for each BBM92 basis while changing the transmission of the channel between the photon source and Bob.

During these measurements, Alice’s channel transmission was fixed at -12 dB.

poled lithium niobate crystal (poling period of  $7.5 \mu\text{m}$ ) that is within a polarizing Sagnac interferometer. This Sagnac entangled photon source [24][25], ignoring time bins, produces the state

$$\frac{(|H\rangle_{810}|H\rangle_{1550} + e^{i\phi}|V\rangle_{810}|V\rangle_{1550})}{\sqrt{2}}. \quad (32)$$

The 532-nm pump has a bandwidth of 64 GHz full-width at half-maximum (FWHM). The peaks (bandwidths) of the downconversion photons are 809.7 nm (0.4 nm) and 1551 nm (1.5 nm). The downconversion bandwidths were measured using difference frequency generation between the pump and a wavelength-tunable 1550-nm laser[26]; the laser wavelength was swept while the counts on the 810-nm side were recorded[27].

The 1550-nm photons were detected using WSi superconducting nanowire detectors from JPL, optimized for 1550 nm with an efficiency of  $\sim 80\%$ [28]. One detector had efficiency of  $\sim 40\%$  due to coupling fiber misalignment after installation, so 3-dB attenuators were added to the fibers entering the other detectors to even out the detection efficiency. Avalanche photodiodes (Excelitas SPCM-AQ4C) with efficiency  $\sim 45\%$  were used to detect the 810-nm

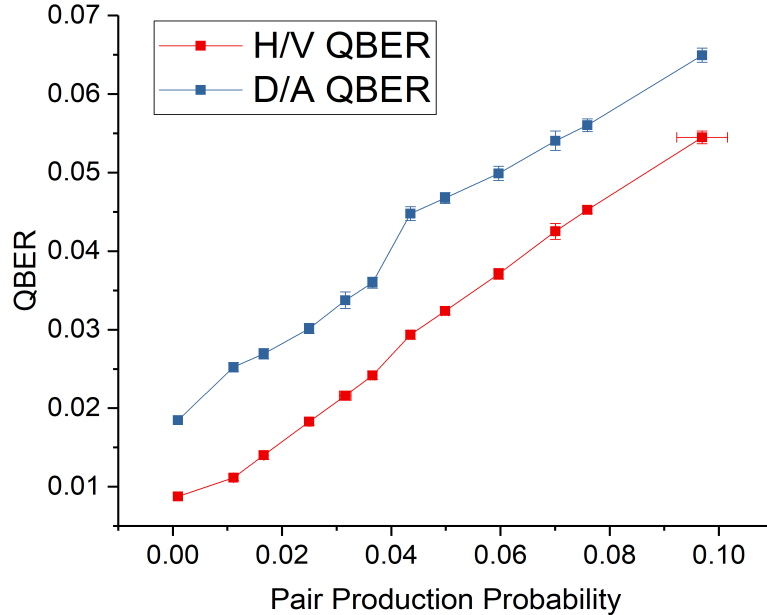


FIG. 11: BBM92 QBER vs Pair Production Probability: Measurement of QBER for each BBM92 basis while changing the pair production probability.

photons.

### Time-bin Phase Stabilization and Calibration

Due to natural environmental factors (vibration, temperature fluctuations), the phase between the time bins is prone to drift; to counteract this we stabilized the phase using an active proportional-integral (PI) feedback[29] system. The phase was measured using some of the pump beam that was also sent (counter-propagating) through the analyzer interferometer in a mode that was vertically displaced from the single-photon beam. The output of the stabilization interferometer was measured using Detectors D1 and D2, low-bandwidth amplified Si photodiodes (Thorlabs PDA36A). Due to the stabilization beam wavelength not matching the design specification of some of the components, and because the low-bandwidth detectors could not distinguish the interfering time bins (e.g., the short (long) path in the pump interferometer and the long (short) path in Alice or Bob’s analyzer interferometer) from the non-interfering ones (short paths in both interferometers and long paths in both interferometers), the visibility was quite low ( $< 10\%$ ) and also different for D1

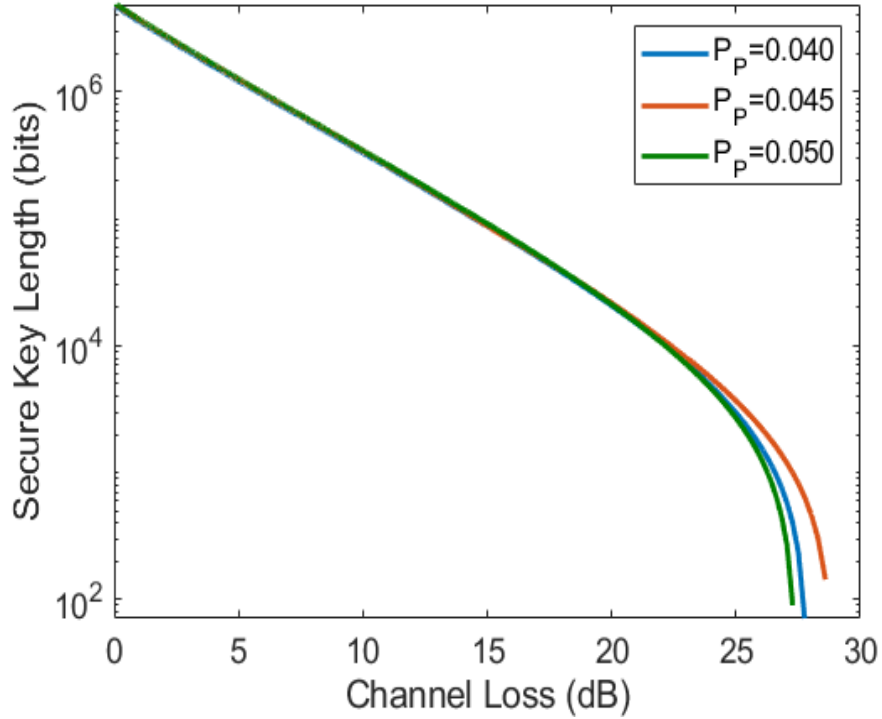


FIG. 12: Finite Key BBM92 Simulation: Secure key length vs channel loss for various pair production probabilities, calculated using the system parameters in S.I. Table II.

and D2. This difference necessitated the use of a scaling factor  $\gamma$  to equalize the amplitude of oscillation between D1 and D2. With this scaling factor, the Error signal,  $E$ , used for the PI feedback algorithm was

$$E \equiv \frac{(I_{D1} - \gamma I_{D2})}{(I_{D1} + \gamma I_{D2})}, \text{ with } \gamma \sim 0.6. \quad (33)$$

The feedback system was designed to keep  $E$  at zero by sending a signal to a piezo-actuated translation stage under the analyzer interferometer's right-angle prism to adjust the phase, at an update rate of 100 Hz. Independent PI systems were implemented for the Pump-Alice combined interferometer and for the Pump-Bob combined interferometer.

Additionally, for QKD it is not only necessary that the phase is kept stable, but also that it is calibrated to the correct value. By changing the phase between  $|H\rangle$  and  $|V\rangle$ , the liquid crystals after Alice's interferometer were used to adjust the phase of states in Basis 2 and 4 so that the photons were routed to the correct detector. For Basis 3 and Basis 4, it was necessary to tilt (about the vertical axes) a QWP before the source to adjust the phase of the polarization-entangled state so that  $|D\rangle$  and  $|A\rangle$  were routed to the correct detectors on

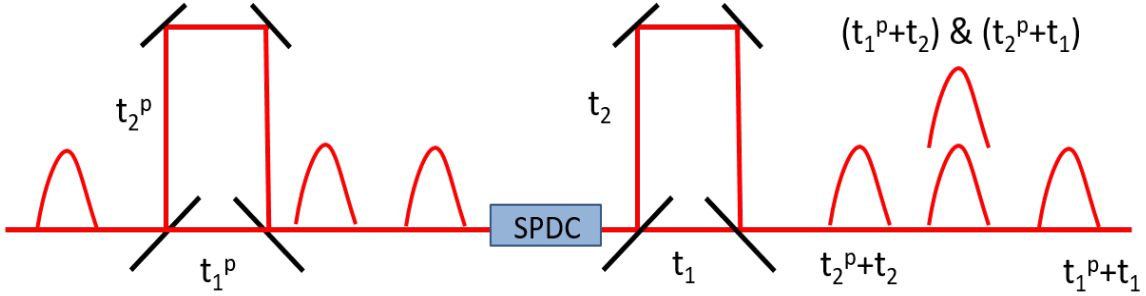


FIG. 13: Franson Time-Bin Qubit Preparation and Measurement: This diagram illustrates how the time bins are created and what possible combinations of them exit the second delay interferometer. Here we assume that  $t_2 - t_1 = t_2^p - t_1^p$ , i.e., that the path-length imbalances are matched. In this case, photons in either of the middle two time bins can interfere.

each side.

### Time-bin Sorting Circuit Operation

As displayed in S.I. Fig. 13, there are three time bins which exit Alice or Bob's time-bin analyzer interferometer, each with a different exit time with respect to the pulse which entered the pump delay interferometer. It is imperative to be able to distinguish all three of these time bins for the HEQKD and BBM92 protocols implemented with this setup. The measurement of time-bin qubits using free-running, single-photon detectors alone lacks the ability to sort bases measurements when events from different time bins are routed to the same detector as in this experiment. It was therefore necessary to develop a circuit which could filter the events corresponding to different time bins into different electrical signals. We used the pump laser as a clock reference and filtered the signals from each detector based on their delay with respect to the laser clock, using an AND gate with a window width of  $\sim 1$  ns. Each time bin has a unique delay with respect to the laser clock so this enabled complete filtering of the time bins.

In the time-bin sorting circuit, each detector output was copied (using ON Semi. NB7VQ14M) three times and was ANDed with a copy of the clock that was delayed by the correct amount so that only events from one of the time bins was successfully transmitted through the AND gate. This process was executed for all eight detectors (four for Alice and

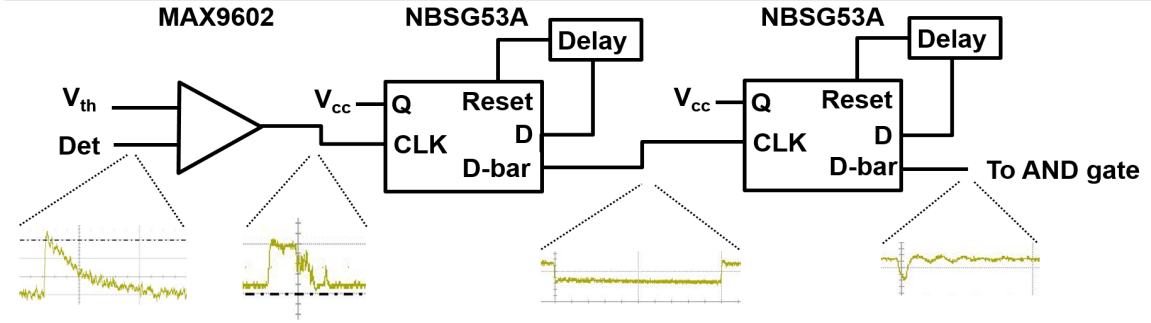


FIG. 14: Time-bin Sorting Circuit: Descriptive schematic of pulse shaping using the MAX9602 high-speed comparator several NBSG53A high-speed D-flip flops with  $\sim 50$  ns delay then a  $\sim 700$  ps delay.

four for Bob) and for all three time bins, creating 24 unique output signals (12 for Alice and 12 for Bob).

To use an AND gate (Analog Devices HMC746LC3C) and adjustable delay chip (ON Semi. MC100EP195B) with low jitter ( $< 100$  ps) and high bandwidth ( $> 1$  GHz), it was necessary to transform the electrical signals from the detectors into signals compatible with high-speed differential logic standards like CML and PECL. This was done using a high-speed comparator (Maxim Int. MAX9602). Additionally, to achieve a subnanosecond pulse so the AND gate had  $\sim 1$  ns acceptance window, the pulses from the detectors were shortened to  $< 1$  ns using a cascade of 2 high-speed D flip-flops (ON Semi. NBSG53A). A pulse shortening effect was created by sending the comparator output into the CLK of the D flip-flop with Q (input) attached to logic HIGH and using a delayed copy of the output as a reset signal after the pulse was sent through the flip-flop. This long pulse was then sent through another D flip-flop with a short reset signal, producing a much shorter pulse ( $\sim 1$  ns) than the detector output pulses ( $\sim 40$  ns). See S.I. Fig. 14 for a pictorial description.

### Event Timetagging

The detection events of Alice and Bob were recorded using separate time-tagging electronic devices (UQDevices UQD-Logic-16, time-bin width 156 ps), synchronized via a common 10-MHz sine-wave clock (Agilent 33250A Function Generator). Also, one channel on each time tagger was connected to a TTL pulse source (National Instruments DAQ USB-6210) through cables of the same length. This allowed the different time offsets of each time

tagger to be measured accurately and subtracted out.

### Doppler Shift

The Doppler shift discussed in this work is a non-negligible phase shift between two closely spaced time bins, simply due to the fact that the source has moved significantly in the  $\sim 1$ -ns interval between the two time bins (S.I. Fig. 17b). There is also a frequency shift on the photons but since

$$\gamma \equiv \frac{1}{\sqrt{1 - \left(\frac{V_{ISS}}{c}\right)^2}} = 1.00000000033, \quad (34)$$

which is quite close to 1 for  $V_{ISS} = 7.7$  km/s, the frequency shift is negligible compared to the photon bandwidth of  $\sim 1$  nm.

The exact phase shift produced through the Doppler effect is dependent on many parameters, including the maximum elevation angle of the orbit during a pass, which changes for subsequent passes and is at a maximum for passes directly overhead. For time bins separated by 1.5 ns, calculations using a simulation of the ISS orbit (with orbit inclination of  $51^\circ$ , 400 km altitude and with longitudinal velocity calculated along the beam path to ground station at  $39^\circ$  latitude) and the relativistic longitudinal Doppler shift equation [30] show, for a representative  $85^\circ$  maximum elevation angle orbit of the International Space Station, an expected shift of

$$\Delta L(t) = \left( \sqrt{\frac{1 + \frac{V_{ISS}(t)}{c}}{1 - \frac{V_{ISS}(t)}{c}}} - 1 \right) (10^{-9} s) c, \quad (35)$$

as displayed in Fig. 17. If acquisition starts and stops at a  $20^\circ$  elevation angle then the total  $\Delta L$  from  $t_{start}$  to  $t_{stop}$  is  $\Delta L(t_{stop}) - \Delta L(t_{start}) = 20 \mu m$ .

We implement an in-lab simulation of this Doppler shift, during our compensation system testing, by moving a piezo-actuated translation stage which controls the position of the pump's right-angle prism with the same distance vs time profile as in S.I. Fig. 17a.



	$(t_1^p + t_1)$				$(t_2^p + t_2) \& (t_1^p + t_2)$				
	A1	A2	A3	A4	A1	A2	A3	A4	
$(t_1^p + t_1)B1$	$ H^p_{t_1, t_1}\rangle  H^p_{t_1, t_1}\rangle$	$ H^p_{t_1, t_1}\rangle  H^p_{t_1, t_1}\rangle$	$ H^p_{t_1, t_1}\rangle  V^p_{t_1, t_1}\rangle$	$ H^p_{t_1, t_1}\rangle  V^p_{t_1, t_1}\rangle$	$ H^p_{t_1, t_1}\rangle  A^p_{t_1, t_2}\rangle$	$ H^p_{t_1, t_1}\rangle  A^p_{t_1, t_2}\rangle$	$ H^p_{t_1, t_1}\rangle  D^p_{t_1, t_2}\rangle$	$ H^p_{t_1, t_1}\rangle  D^p_{t_1, t_2}\rangle$	H/V basis
B2	$ H^p_{t_1, t_1}\rangle  H^p_{t_1, t_1}\rangle$	$ H^p_{t_1, t_1}\rangle  H^p_{t_1, t_1}\rangle$	$ H^p_{t_1, t_1}\rangle  V^p_{t_1, t_1}\rangle$	$ H^p_{t_1, t_1}\rangle  V^p_{t_1, t_1}\rangle$	$ H^p_{t_1, t_1}\rangle  A^p_{t_1, t_2}\rangle$	$ H^p_{t_1, t_1}\rangle  A^p_{t_1, t_2}\rangle$	$ H^p_{t_1, t_1}\rangle  D^p_{t_1, t_2}\rangle$	$ H^p_{t_1, t_1}\rangle  D^p_{t_1, t_2}\rangle$	D/A basis
B3	$ V^p_{t_1, t_1}\rangle  H^p_{t_1, t_1}\rangle$	$ V^p_{t_1, t_1}\rangle  H^p_{t_1, t_1}\rangle$	$ V^p_{t_1, t_1}\rangle  V^p_{t_1, t_1}\rangle$	$ V^p_{t_1, t_1}\rangle  V^p_{t_1, t_1}\rangle$	$ V^p_{t_1, t_1}\rangle  A^p_{t_1, t_2}\rangle$	$ V^p_{t_1, t_1}\rangle  A^p_{t_1, t_2}\rangle$	$ V^p_{t_1, t_1}\rangle  D^p_{t_1, t_2}\rangle$	$ V^p_{t_1, t_1}\rangle  D^p_{t_1, t_2}\rangle$	Different bases
B4	$ V^p_{t_1, t_1}\rangle  H^p_{t_1, t_1}\rangle$	$ V^p_{t_1, t_1}\rangle  H^p_{t_1, t_1}\rangle$	$ V^p_{t_1, t_1}\rangle  V^p_{t_1, t_1}\rangle$	$ V^p_{t_1, t_1}\rangle  V^p_{t_1, t_1}\rangle$	$ V^p_{t_1, t_1}\rangle  A^p_{t_1, t_2}\rangle$	$ V^p_{t_1, t_1}\rangle  A^p_{t_1, t_2}\rangle$	$ V^p_{t_1, t_1}\rangle  D^p_{t_1, t_2}\rangle$	$ V^p_{t_1, t_1}\rangle  D^p_{t_1, t_2}\rangle$	
$((t_2^p + t_2) \& (t_1^p + t_2))B1$	$ A^p_{t_1, t_2}\rangle  H^p_{t_1, t_1}\rangle$	$ A^p_{t_1, t_2}\rangle  H^p_{t_1, t_1}\rangle$	$ A^p_{t_1, t_2}\rangle  V^p_{t_1, t_1}\rangle$	$ A^p_{t_1, t_2}\rangle  V^p_{t_1, t_1}\rangle$	$ A^p_{t_1, t_2}\rangle  A^p_{t_1, t_2}\rangle$	$ A^p_{t_1, t_2}\rangle  A^p_{t_1, t_2}\rangle$	$ A^p_{t_1, t_2}\rangle  D^p_{t_1, t_2}\rangle$	$ A^p_{t_1, t_2}\rangle  D^p_{t_1, t_2}\rangle$	
B2	$ A^p_{t_1, t_2}\rangle  H^p_{t_1, t_1}\rangle$	$ A^p_{t_1, t_2}\rangle  H^p_{t_1, t_1}\rangle$	$ A^p_{t_1, t_2}\rangle  V^p_{t_1, t_1}\rangle$	$ A^p_{t_1, t_2}\rangle  V^p_{t_1, t_1}\rangle$	$ A^p_{t_1, t_2}\rangle  A^p_{t_1, t_2}\rangle$	$ A^p_{t_1, t_2}\rangle  A^p_{t_1, t_2}\rangle$	$ A^p_{t_1, t_2}\rangle  D^p_{t_1, t_2}\rangle$	$ A^p_{t_1, t_2}\rangle  D^p_{t_1, t_2}\rangle$	
B3	$ D^p_{t_1, t_2}\rangle  H^p_{t_1, t_1}\rangle$	$ D^p_{t_1, t_2}\rangle  H^p_{t_1, t_1}\rangle$	$ D^p_{t_1, t_2}\rangle  V^p_{t_1, t_1}\rangle$	$ D^p_{t_1, t_2}\rangle  V^p_{t_1, t_1}\rangle$	$ D^p_{t_1, t_2}\rangle  A^p_{t_1, t_2}\rangle$	$ D^p_{t_1, t_2}\rangle  A^p_{t_1, t_2}\rangle$	$ D^p_{t_1, t_2}\rangle  D^p_{t_1, t_2}\rangle$	$ D^p_{t_1, t_2}\rangle  D^p_{t_1, t_2}\rangle$	
B4	$ D^p_{t_1, t_2}\rangle  H^p_{t_1, t_1}\rangle$	$ D^p_{t_1, t_2}\rangle  H^p_{t_1, t_1}\rangle$	$ D^p_{t_1, t_2}\rangle  V^p_{t_1, t_1}\rangle$	$ D^p_{t_1, t_2}\rangle  V^p_{t_1, t_1}\rangle$	$ D^p_{t_1, t_2}\rangle  A^p_{t_1, t_2}\rangle$	$ D^p_{t_1, t_2}\rangle  A^p_{t_1, t_2}\rangle$	$ D^p_{t_1, t_2}\rangle  D^p_{t_1, t_2}\rangle$	$ D^p_{t_1, t_2}\rangle  D^p_{t_1, t_2}\rangle$	

FIG. 16: BBM92 Coincidence Matrix: Coincidence matrix of all detector and time-bin combinations used in the BBM92 protocol demonstration. See S.I. Fig. 13 for pictorial

definition of time bins  $t_1^p + t_1$ ,  $(t_1^p + t_2 \& t_2^p + t_1)$ , and  $t_2^p + t_2$ , where

$$(t_1^p + t_2 \& t_2^p + t_1) = t_{2(1)}^p + t_{1(2)}.$$

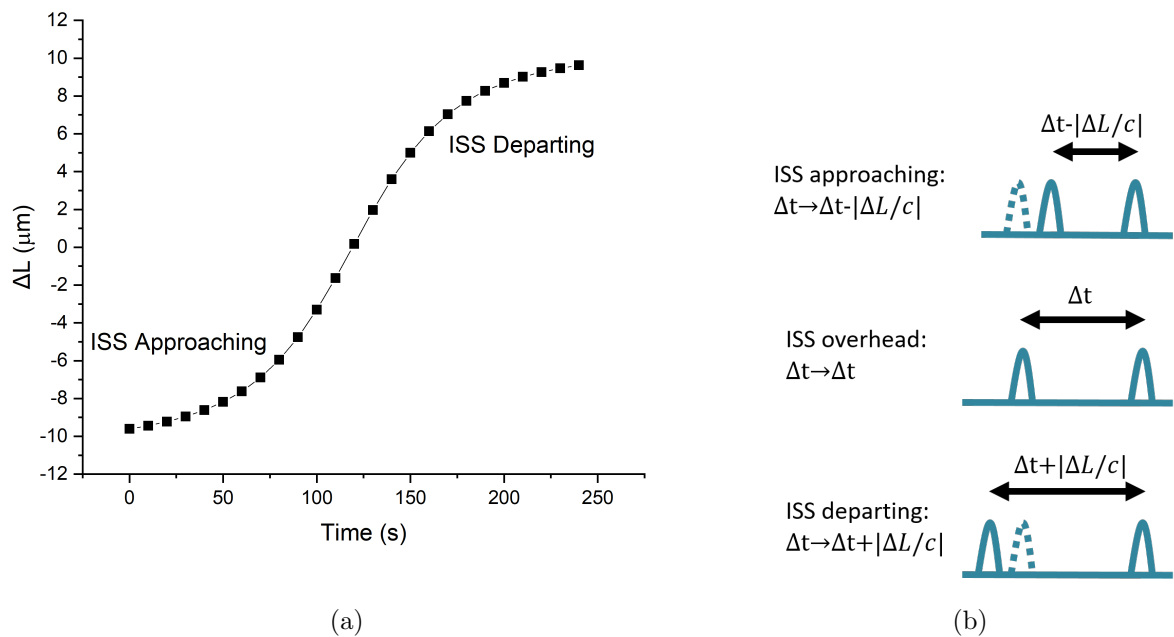


FIG. 17: Expected Doppler Shift: (a) Expected Doppler shift for overhead orbit of the International Space Station. (b) Pictorial explanation of effect of Doppler shift on time bins.